Polymer Chemistry

ROYAL SOCIETY OF CHEMISTRY

PAPER

View Article Online
View Journal | View Issue

Cite this: *Polym. Chem.*, 2025, **16**, 4961

Reactive oxygen species-sensitive thioether-bearing poly(2-oxazoline)s: direct and controlled polymerization using an initiator salt

Saba Nemati Mahand,[a] Anna-Lena Ziegler,[a] Parsa Amin,[b] Florian T. Kaps[a] and Robert Luxenhofer *[a]

Reactive oxygen species (ROS)-responsive polymers have attracted significant attention for their potential in biomedical applications, particularly in drug delivery and tissue engineering. This study presents the first direct synthesis and characterization of ROS-responsive thioether-bearing poly(2-oxazoline)s *via* controlled cationic ring-opening polymerization. Typical initiators have been shown to lead to loss of control over the polymerization of 2-(methylthio)-methyl-2-oxazoline. Here we show that its controlled polymerization is possible *via* the initiator salt method. The living character was confirmed by kinetic experiments and chain extension, used to synthesize amphiphilic block copolymers. Their ROS-responsiveness was evaluated through *in vitro* studies in the presence of hydrogen peroxide. The amphiphilic self-assemblies disassemble over time, as demonstrated for a triblock copolymer, suggesting a significant change of hydrophilicity of the polymer upon exposure to ROS. Together, the presented synthetic approach has much better atom economy than a previously published approach and enables facile and direct access to ROS-responsive POx with more complex architectures.

Received 2nd July 2025,
Accepted 1st October 2025

DOI: 10.1039/d5py00659g

rsc.li/polymers

Introduction

Over the last few decades, considerable efforts have been made to develop advanced stimuli-responsive polymers to enhance the therapeutic efficacy of drug,[1–3] protein or gene[4–6] delivery systems while reducing side effects.[7,8] Stimuli-responsive systems can be categorized into three groups: those sensitive to physical stimuli (temperature, light, mechanical stress, electrical/magnetic field, and ultrasound),[9,10] chemical stimuli (glucose, pH, ionic strength, and reactive oxygen species (ROS)),[11–13] or biochemical stimuli (enzymes and antigen antibodies).[14–18] Among these stimuli, ROS, such as hydrogen peroxide (H_2O_2), hydroxyl radicals ($^{\bullet}OH$), superoxide ($O_2^{\bullet-}$), and singlet oxygen ($^1O_2$) form an interesting niche in designing responsive micelles.[19] When an organism is injured, H_2O_2 production is upregulated through multiple biochemical processes.[20] Disruption in mitochondrial respiration exacerbates the leakage of electrons from the electron transport chain, as well as the formation of $O_2^{\bullet-}$, which is then converted into H_2O_2 by superoxide dismutase. Additionally, H_2O_2 is produced by NADPH and xanthine oxidases in the injured tissue.[21,22] Importantly, H_2O_2 is uncharged and comparatively stable in aqueous solutions, facilitating its diffusion across cell membranes for cellular signaling at sites distant from its origin.[23] While H_2O_2 concentration in healthy tissue is less than 10 nM, it can exceed 100 μM in inflamed tissues, which represents a four orders of magnitude increase in its concentration under pathological conditions.[24,25] While the pH value and temperature also change with inflammation, the changes are minute in comparison. Considering the diffusion gradient of H_2O_2, which extends 100–200 μm from the inflamed tissue site,[20,24] and the concentration difference between healthy and inflamed tissues, ROS-responsive polymers could be suitable candidates for drug release specifically to inflamed tissues.

Recent studies have shown considerable advancements in the development of smart delivery systems that release therapeutic agents in response to ROS.[26,27] These systems typically utilize the oxidation of hydrophobic components to form highly hydrophilic polymeric materials. This transformation promotes the controlled release of the encapsulated therapeutic agents.[28] Various ROS-responsive groups, such as thioether,[29–31] telluride,[32] alkyl diselenide,[33] arylboronic ester,[34] thioketal,[35] oligoproline,[36] and peroxalate ester,[37] are available. Among these, thioether-bearing groups have been extensively studied in the biomedical field due to the hydrophobic to hydrophilic transition upon oxidation.[38,39]

[a]*Soft Matter Chemistry, Department of Chemistry, and Helsinki Institute of Sustainability Science, Faculty of Science, University of Helsinki, 00560 Helsinki, Finland. E-mail: robert.luxenhofer@helsinki.fi*
[b]*School of Engineering Science, LUT University, 53850 Lappeenranta, Finland*

Poly(2-oxazoline)s (POx) are a polymer class that has garnered some interest in the design of functional biomaterials.[40,41] The increasing popularity of POx in the biomedical field is based on the combination of relatively easy and controllable synthesis and high synthetic diversity[42,43] with good cytocompatibility[44] and biocompatibility.[45–47] POx are typically synthesized *via* cationic ring-opening polymerization (CROP) of 2-substituted-2-oxazolines. The 2-substituent of the 2-oxazoline monomers defines the POx side chains and is therefore decisive for the polymer's physicochemical properties.[48] Using suitable reaction conditions, the CROP of 2-oxazolines can proceed in a (quasi-)living manner, thereby enabling the synthesis of polymers with controllable molecular weights and narrow molar mass distributions.[49] Consequently, block copolymers can be realized by sequential monomer addition,[43] thus providing access to a large variety of amphiphiles that are capable of forming diverse forms of self-assemblies.[50] Also gradient copolymers can function as nanocarrier systems for drug delivery.[51]

Thioether-containing POx have been considered for ROS-responsive applications.[52] For instance, the POx homopolymer poly(2-(methylthio)methyl-2-oxazoline) (PMeSMeOx) is hydrophobic due to the thioether side chain but turns hydrophilic upon sulfur oxidation. This feature allows one to design micellar systems that disassemble in the presence of ROS.[52] For this, block copolymers based on PMeSMeOx and a hydrophilic polymer such as poly(2-methyl-2-oxazoline) (PMeOx) or polyethylene glycol (PEG) are required. However, synthesizing thioether-containing POx in a controlled manner remains a challenging task. Kempe *et al.* reported that common CROP initiators, such as methyl *p*-toluenesulfonate (methyl tosylate) and methyl trifluoromethanesulfonate (methyl triflate), do not enable a controlled CROP of the monomer 2-(methylthio) methyl-2-oxazoline (MeSMeOx).[53] Upon polymerization, the molecular weight does not increase linearly with conversion but shows an initial steep increase, after which it remains relatively constant, suggesting very significant chain transfer. Likely, this is due to the nucleophilic character of the thioether moiety. In particular, the effective initiation of the polymerization may be compromised by a nucleophilic attack of the sulfur on the initiator. Accordingly, to realize defined PMeSMeOx, Bener *et al.* used a 3-step procedure comprising the synthesis of poly(2-ethyl-2-oxazoline) (PEtOx), its complete hydrolysis to polyethylene imine (PEI) and the subsequent reacylation with 2-(methylthio)acetic acid.[52] However, while effective, this approach is rather laborious and wasteful and does not allow facile block copolymer synthesis *via* sequential monomer addition but requires alternative techniques such as polymer coupling, which can pose significant challenges.

In the present work, we report an approach for directly polymerizing MeSMeOx using an oxazolinium salt initiator, namely *N*-methyl-2-methyl-2-oxazolinium triflate (MeMeOxOTf). This allows for the first time a quasi-living CROP of MeSMeOx, as confirmed by kinetic investigations. Thus, defined ROS-responsive PMeSMeOx homopolymers and an amphiphilic MeOx/MeSMeOx-based gradient copolymer are obtained with reasonably narrow molar mass distributions and controlled degrees of polymerization (DP). In addition, ROS responsive block copolymers are synthesized by one-pot sequential monomer addition. Accordingly, we introduce amphiphilic PMeSMeOx/PMeOx copolymers of different architectures capable of self-assembling into micellar aggregates. The polymers show good cytocompatibility with IC_{50} values exceeding 10 g L^{-1}. In addition, we demonstrate their ROS-responsive behavior by treatment with H_2O_2. Taken together, we present here a facile route to overcome synthesis limitations of ROS-responsive POx suitable for future biomedical applications.

Materials and methods

(Methylthio)acetonitrile (99%) was procured from Thermo Scientific Chemicals (Finland), while 1-Boc-piperazine (Boc-Pip, 98%) was sourced from Fluorochem (United Kingdom). 2-Methyl-2-oxazoline (MeOx) was obtained from abcr GmbH (Germany). Additional reagents, including 2-aminoethanol, methyl trifluoromethanesulfonate (methyl triflate, MeOTf), methanol, diethyl ether, acetonitrile, chlorobenzene, calcium hydride (CaH_2), phosphorus pentoxide (P_2O_5), and zinc acetate dihydrate, were purchased from Sigma-Aldrich. All chemicals were used as received unless specified otherwise.

MeOx and synthesized 2-(methylthio)methyl-2-oxazoline (MeSMeOx) were dried by refluxing over CaH_2 under a nitrogen atmosphere, followed by distillation prior to use. Acetonitrile was dried by refluxing over P_2O_5 under a nitrogen atmosphere, followed by distillation prior to use.

Synthetic procedures

The monomer MeSMeOx was synthesized based on a procedure by Witte and Seeliger.[53,54] In brief, the catalyst (zinc acetate, 0.02 equiv.) was added to the nitrile ((methylthio) acetonitrile, 1 equiv.) and heated to 130 °C, after which 2-aminoethanol (1.2 equiv.) was added dropwise to the suspension. The reaction mixture was refluxed until a 99% conversion of the reagent (methylthio)acetonitrile was achieved, as monitored by ^{1}H NMR spectroscopy. The reaction mixture was cooled down to ambient temperature and washed once with brine and twice with H_2O. The organic phase was dried over $MgSO_4$. Upon filtration, the solvent was evaporated under reduced pressure. The crude product was dried with CaH_2 overnight and distilled and fractionated under an inert atmosphere with reduced pressure to yield the product as a colorless liquid (Scheme S1). More detailed information on the monomer synthesis and characterization is given in the SI (Tables S1 and Fig. S1).

The initiator salt *N*-methyl-2-methyl-2-oxazolinium triflate (MeMeOxOTf) was synthesized based on a protocol by Kobayashi *et al.*[55] Briefly, MeOx (1 equiv.) and methyl triflate (MeOTf, 1.1 equiv.) were added to diethyl ether (4×10^{-3} wt%) under an inert atmosphere and stirred at −10 °C for 2 h. The resulting salt initiator MeMeOxOTf was dried *in vacuo* for 2 h, washed with fresh diethyl ether, and again dried *in vacuo*

(Scheme S1). The salt initiator reaction was controlled by ^{1}H-NMR spectroscopy. The synthesized initiator was dissolved in acetonitrile prepared for use in polymerization. More details regarding the synthesis can be found in the SI (Table S2 and Fig. S2).

All polymerizations and work-up procedures were carried out after a general procedure described previously.[53,56–59] Briefly, the MeMeOxOTf or MeOTf initiators (1 equiv.), for homopolymers, gradient polymers and copolymers, were added to a dried Schlenk flask under an inert atmosphere and dissolved in the respective amount of acetonitrile. For homopolymers ($PMeSMeOx_{20}$ (**P1**), $PMeSMeOx_{60}$ (**P2**), $PMeSMeOx_{110}$ (**P3**)), MeSMeOx (20, 60 or 110 equiv.) was added, and the reaction mixture was heated to 80 °C and stirred until complete consumption of the monomer, as monitored by ^{1}H-NMR spectroscopy. Similarly, for the gradient copolymer ($P(MeOx_{70}$-$MeSMeOx_{20})_{grad}$ (**P4**)), both monomers MeOx and MeSMeOx were added to the salt initiator MeMeOxOTf before heating to 80 °C. For the diblock copolymer synthesis ($PMeOx_{70}$-*b*-$PMeSMeOx_{20}$ (**P5**)), the monomer for the first block (MeOx) was added to the mixture of the initiator MeOTf and solvent. The reaction mixture was heated to 80 °C and stirred until complete consumption of the monomer, as monitored by ^{1}H-NMR spectroscopy. After the consumption of MeOx, the mixture was cooled to room temperature and the monomer for the second block (MeSMeOx) was added. The mixture was heated to 80 °C overnight. For the triblock copolymer synthesis ($PMeOx_{35}$-*b*-$PMeSMeOx_{20}$-*b*-$PMeOx_{35}$ (**P6**)), the same procedure was repeated with the monomer for the third block (MeOx). For all polymerizations, the terminating reagent Boc-Pip (3 equiv.) was added after confirmation of full monomer consumption by ^{1}H-NMR and the reactions were stirred at 50 °C overnight. The solvent was removed under reduced pressure and the crude polymers were precipitated three times from methanol into diethyl ether, followed by drying under vacuum (Scheme S1). More details regarding the synthesis and characterization can be found in the SI (Table S3 and Fig. S3–S6).

Polymer characterization

The ^{1}H-NMR spectra were obtained using a Bruker Biospin Avance III 500 MHz spectrometer (Germany) at 25 °C (298 K). The spectra were calibrated based on the residual protonated solvent ($CDCl_3$) signal at 7.26 ppm. Data analysis was carried out using Bruker Topspin 4.1.3 software.

Size Exclusion Chromatography (SEC) was carried out with equipment from Polymer Standard Service (PSS, Mainz, Germany). The setup included a precolumn (50 × 8 mm, PSS PFG linear M) and two columns (300 × 8 mm, PSS PFG linear M, particle size 7 μm, pore size 0.1–1000 kDa) operating at 40 °C (313 K). The HFIP eluent was supplemented with 3 g L^{-1} potassium triflate, and the flow rate was maintained at 0.5 mL min^{-1}. Samples were filtered through 0.22 μm PTFE syringe filters prior to each measurement.

A Shimadzu IRTracer-100 infrared spectrophotometer was used to conduct infrared spectroscopy at room temperature. The samples were ground into a fine powder for preparation, and the spectra were recorded from 600 to 4000 cm^{-1}. A Mettler Toledo React IR TM 15 was used for the *in situ* IR measurements with a 6.3 mm AgX DiComp as the probe.

Matrix-assisted laser desorption ionization time of flight mass spectrometry (MALDI-TOF-MS) measurements were performed using a Shimadzu AXIMA Performance MALDI-TOF mass spectrometer. For sample preparation, 15 μL of the polymer solution (c = 10 g L^{-1} in methanol) and 9 μL of the NaTFA solution (c = 10 g L^{-1} in methanol) were added to 5 μL of a solution of DT (c = 100 g L^{-1} in THF) and rapidly mixed with the pipette tip. Two times 0.5 μL of the mixture were spotted onto a stainless-steel target plate. Measurements were carried out in the reflector mode. Calibration was performed using PEG-2k standards.

The thermal stability of the polymers was evaluated using thermogravimetric analysis (TGA), with a NETZSCH STA 449F5. The samples, weighing between 10 and 20 mg, were heated from 30 to 600 °C under a nitrogen and normal atmosphere at a rate of 10 °C min^{-1}. Differential Scanning Calorimetry (DSC) was conducted with a TA Instruments DSC Q2000 calorimeter, using a nitrogen purge gas at 50 mL min^{-1}. Approximately 4 mg of each sample was sealed in aluminum pans. DSC analysis was carried out with a heating–cooling–heating cycle from −40 °C to 200 °C at a heating and cooling rate of 10 °C min^{-1}. The glass transition temperature (T_g) values were obtained from the second heating run.

To facilitate uniform micelle formation with consistent size, polymeric micelles were prepared by initially dissolving 10 mg of the polymer in 1 mL of methanol in 1.5 mL microcentrifuge tubes (Eppendorf). The solution was heated to 37 °C in a thermomixer for 5 minutes to support complete dissolution. Subsequently, methanol was removed under a stream of nitrogen for 15 minutes. Further drying was carried out by rotary evaporation for 20 minutes. The resulting thin film was rehydrated by adding an equal volume of diH_2O (2 mM $NaNO_3$) and mixing with a thermomixer for an additional 10 minutes to ensure uniform polymer dispersion in diH_2O at a concentration of 1 g L^{-1} (Scheme S2).

Before performing dynamic light scattering (DLS) measurements, polymer micelle solutions were filtered through a hydrophilic 0.45 μm PTFE syringe filter to remove any large aggregates or impurities and transferred to disposable cuvettes. The size distribution of the polymeric micelles was assessed using a DLS instrument, which is composed of a BI-200SM goniometer, a BIC-TurboCorr digital pseudo-cross-correlator and a BI-CrossCorr detector, equipped with two BIC-DS1 detectors, all of which were manufactured by Brookhaven Instruments Corporation. The light source consisted of a Sapphire 488-100 CDRH laser (Coherent GmbH) operated at λ_0 = 488 nm and its power adjustment system (range: 10–50 mW). The size of the pinhole before the detector was set to 2 mm. Measurements were carried out at 45° scattering vectors. The measurements were recorded as the average of three test runs for one individually prepared sample. Data processing was carried out using the program dynamic light scattering software by Brookhaven Instruments.

To prepare the polymer for scanning electron microscopy (SEM) investigations, it was first dissolved in diH_2O at a concentration of 1 g L^{-1}. The solution was spin coated on a glass slide. Subsequently, the dried samples were mounted on aluminum sample holders using conductive carbon tape. They were then sputter-coated with gold using a BOC Edwards sputter coater to enhance electrical conductivity and prevent specimen charging under the electron beam. The gold coating was applied at a current density of 40 mA and a voltage of 1.5 kV for 8 minutes. The morphology of the particles was studied qualitatively with a scanning electron microscope (Hitachi SU 3500, Tokyo, Japan) at an acceleration voltage of 20 kV under high vacuum conditions.

For transmission electron microscopy (TEM) investigations, previously freeze-dried polymer micelles were dissolved in MilliQ H_2O to a concentration of 20 g L^{-1}. Copper grids (200 mesh) with a pioloform film and carbon coating were glow-discharged for 15 s on an Emitech glow discharge system operated at 25 mA. Polymer samples were diluted (1/125) and 8 μL were incubated on the grids for 1 min before blotting. The grids were washed three times with 15 μL deionized water and then blotted. For negative staining, the grids were incubated with 8 μL 2% uranyl acetate for 3 min, blotted, washed with 8 μL H_2O and blotted. Grids were further allowed to dry on filter paper. Imaging was performed on a Hitachi HT7800 microscope (Hitachi High-Technologies) operated at 100 kV and equipped with a Rio9 bottom mounted CMOS camera (Gatan, Inc.).

Asymmetric flow field-flow fractionation (AF4) was carried out on a Wyatt Eclipse AF4 separation system equipped with UV/Vis (Agilent 1260 Infinity VWD, Agilent), refractive index (dRI) (Optilab rex, 633 nm, Wyatt), and multiangle laser light scattering (MALLS) (Dawn Heleos-II, 663 nm, Wyatt) detectors and a 1260 Bio Quat Pump and 1260 ALS autosampler (Agilent). The UV/Vis detector was set to a wavelength of 250 nm. The measurements were carried out at room temperature in a Wyatt long channel equipped with a 350 μm spacer and a membrane of regenerated cellulose with a molecular weight cut-off of 10 kDa serving as an accumulation wall. A filtered solution of 50 mM $NaNO_3$ and 5 mM NaN_3 in deionized water was used as the eluent. Samples were dissolved in the eluent to achieve a concentration of 10 mg mL^{-1} and subsequently diluted to a final concentration of 1 mg mL^{-1}. Sample solutions were filtered through a 0.45 μm PTFE syringe before the measurement. The injected volume was 50 μL. Separation was carried out using an exponential crossflow profile (Fig. S13b). The measurement data were analyzed using the Astra 7 software (Wyatt).

To study ROS induced oxidation, PMeSMeOx20 (**P1**) was incubated with 4 different concentrations of H_2O_2 (H_2O as the control, 10 nM, 100 μM, and 10 mM) (polymer concentration: 10 g L^{-1}). Oxidation was monitored using ^{1}H NMR, SEC, and IR after a 5-day incubation. Additionally, changes in the self-assembly behavior of $PMeOx_{35}$-*b*-$PMeSMeOx_{20}$-*b*-$PMeOx_{35}$ (**P6**) were assessed by tracking variations in light scattering intensity over time by incubation in the presence of H_2O_2 (H_2O as the control, 10 nM, 100 μM, and 10 mM).

Polymer cytotoxicity

The *in vitro* cell viability studies were carried out using the luminescent CellTiter-Glo® (Promega Corp., Madison, WI) assay employing the NIH 3T3 cell line from ACCT (CRL-1658) (USA). Two different passages of NIH 3T3 cells (representing two different biological replicates) were seeded in 96-well plates (Corning® 3610, Corning, NY) at a density of 5000 cells per well in 100 μL Dulbecco's modified Eagle's medium (DMEM). The cells were allowed to adhere overnight at 37 °C, 5% CO_2, and 95% relative humidity. The medium was discarded and replaced with 100 μL of copolymers dissolved in the medium at concentrations ranging from 0.0003 to 10 wt% (n = 3; technical replicates per polymer). Cells treated with 100 μL Triton™ X-100 (100 μL mL^{-1}) served as a cytotoxic positive control group and cells incubated with DMEM served as the negative control group. The cells were incubated at 37 °C, 5% CO_2, and 95% relative humidity for periods of 24 and 72 h. The cells were washed twice with phosphate buffered saline (PBS). Then, 50 μL of both PBS and CellTiter-Glo® assay reagent were added to each well. The plates were gently shaken for 2 min, followed by a 30-minute incubation at room temperature in the dark. Luminescence was then determined using a Varioskan LUX multimode microplate reader (Thermo Fisher Scientific, Inc.). Cell viability was calculated using eqn (1):

$$\text{Cell viability} = \frac{V_P - AV_B}{AV_{NC} - AV_B} \times 100, \quad (1)$$

where AV_{NC} and AV_B are the absorption values of the average of the negative control group samples and the blank measurement medium, respectively (n = 3, three technical replicates). V_P is the absorption value of the respective polymer-treated samples (PBS/CellTiter-Glo® assay reagent = 1 : 1 (v : v)). The final viabilities were calculated as mean ± standard deviation (SD) (n = 6, 2 biological replicates × 3 technical replicates).

Results

The monomer 2-(methylthio)methyl-2-oxazoline (MeSMeOx) was synthesized in a one-pot reaction from commercially available compounds following a previously published protocol,[53] based on the Witte and Seeliger procedure.[60] Success of the synthesis was confirmed by ^{1}H NMR (Fig. S1). More details regarding the monomer synthesis and characterization can be found in the SI.

MeSMeOx has been synthesized and polymerized before. However, Kempe *et al.*[53] reported that PMeSMeOx could not be polymerized in dichloromethane in a controlled way using the common POx initiators methyl tosylate and methyl triflate. Similarly, we were not able to polymerize MeSMeOx *via* CROP in acetonitrile using the methyl triflate initiator, and no polymer was obtained (Scheme 1a). Kempe *et al.* hypothesized that the lack of control in the CROP is due to the nucleophilic character of sulfur inducing side reactions instead of polymerization. Therefore, Bener and co-workers recently introduced a rather elaborate 3-step approach to prepare the defined

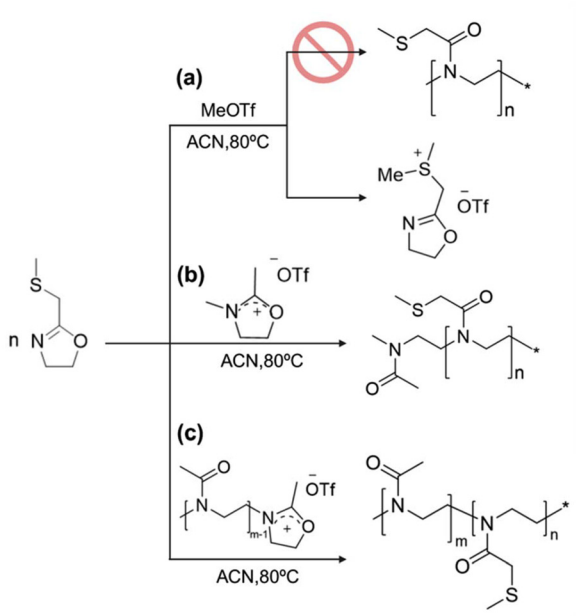

Scheme 1 Schematic representation of (a) the unsuccessful CROP of MeSMeOx when using common CROP initiators, (b) the utilization of the salt initiator MeMeOxOTf, which, in contrast, allows the CROP of MeSMeOx and (c) the synthesis of a MeOx/MeSMeOx diblock copolymer, which can be conducted similarly.

PMeSMeOx, which included the synthesis of poly(2-ethyl-2-oxazoline) (PEtOx), its exhaustive hydrolysis to polyethylenimine (PEI) and the subsequent modification *via* acylation with 2-(methylthio)acetic acid.[52] However, this approach is wasteful with an atom economy of less than 10%. Here, we utilize a somewhat unique feature of the 2-oxazoline/2-oxazine CROP. When stoichiometric amounts of initiator MeOTf and monomer, here 2-methyl-2-oxazoline (MeOx), are combined at low temperature, an initiator salt can be easily isolated, namely, *N*-methyl-2-methyl-2-oxazolinium triflate (MeMeOxOTf) (Fig. S2). This so-called initiator salt is essentially the relatively stable propagating species of the CROP. We hypothesized that compared to the highly electrophilic CROP initiators methyl triflate or methyl tosylate, which can readily react with the sulfur of the MeSMeOx monomer, the initiator salt is much less reactive, thus avoiding sulfur-related side reactions (Scheme 1b). Being the active species, it is, however, able to carry out the propagation reaction. Similarly, MeSMeOx should be readily employable to the chain extension of a living PMeOx (or alternative POx) polymer (Scheme 1c). Thus, PMeSMeOx-based block copolymers should be feasible by living CROP *via* sequential monomer addition.

First, we set out to demonstrate control over the degree of polymerization of PMeSMeOx homopolymers using the salt initiator approach. The degrees of polymerization of 20 (**P1**), 60 (**P2**), and 110 (**P3**) were targeted. The same approach was used for the copolymerization of MeOx and MeSMeOx to realize P(MeOx-*co*-MeSMeOx) (**P4**). In addition, to address more advanced polymer structures, we used MeSMeOx to chain extend living PMeOx blocks, thus realizing a $PMeOx_{70}$-*b*-$PMeSMeOx_{20}$ diblock (**P5**) and a $PMeOx_{35}$-*b*-$PMeSMeOx_{20}$-*b*-$PMeOx_{35}$ triblock copolymer (**P6**). For these block copolymer syntheses, no initiator salt was required. All polymerizations were terminated using 1-Boc-piperazine (Fig. 1a).

The polymers were analyzed by ^{1}H NMR, IR, and SEC. Signals observed in the ^{1}H NMR spectra are in good agreement with the expected polymer structure (Fig. S3–S6). Furthermore, the ^{1}H NMR spectra allowed us to determine the DPs and the number-average molecular weights $M_{n,NMR}$ by end-group analysis. The determined values are in good agreement with the targeted ones for all polymers (Table 1). The IR spectra of the polymers show a prominent band at about 800 cm^{-1}, characteristic of C–S stretching (Fig. S7). Characterization of the polymers by SEC revealed essentially monomodal molar mass distributions of the polymers (Fig. 1b and c). Comparison of homopolymers **P1–P3** shows the expected SEC peak shift towards smaller elution times with increasing target molar mass (Fig. 1b). Elugrams of the copolymers **P4–P6**, in turn, are closely aligned, as expected based on their identical targeted DP and MeOx : MeSMeOx ratio (Fig. 1c). Molar mass distributions are narrow to moderate for the homopolymers ($1.2 < Đ < 1.4$) and somewhat narrower for the copolymers ($1.2 < Đ < 1.3$). A low molar mass shoulder distribution is clearly observed for **P6**. The higher-than-expected number-average molecular weights $M_{n,SEC}$ as obtained from SEC are readily attributed to the conventional calibration using PMMA standards. Furthermore MALDI-TOF mass spectrometry was performed for **P1** (Fig. S8). Analysis of the mass spectrum shows a major distribution and several minor ones. The mass distribution peaks at around 1200 m/z, which is significantly lower than expected, as it would correspond to a DP of only 7–8. Although not commonly observed so profoundly for POx, we tentatively attribute this to mass discrimination possible in Maldi-ToF mass spectrometry, as NMR and SEC analyses do not suggest such low DP. All distributions show a peak-to-peak distance of $\Delta m/z = 131$, which corresponds to the mass of the repeat unit. The most abundant distribution (α-distribution, Fig. S8) can be attributed to polymer chains initiated with a proton, ionized by sodium and terminated with piperazine. The proton initiation can be attributed to chain transfer. The terminal piperazine is likely a result of Boc removal during ionization. The β-distribution can be attributed to an initiator-salt initiated polymer with either water termination or a chain end originating from chain transfer. In contrast, the distributions γ and δ can be attributed to polymer chains with the correct initiator and termination moiety (Fig. S8).

Accordingly, the mass spectrum suggests the occurrence of chain transfer during the polymerization. However, the mass spectra could overemphasize the corresponding species, *i.e.* proton initiated chains (Fig. S8); if chain transfer were dominant as suggested by MALDI, kinetic experiments (*vide infra*, Fig. 2) should clearly show it. In any case, analyses by NMR, IR, SEC, and MALDI-TOF mass spectrometry indicate successful syntheses of the polymers. More information regarding

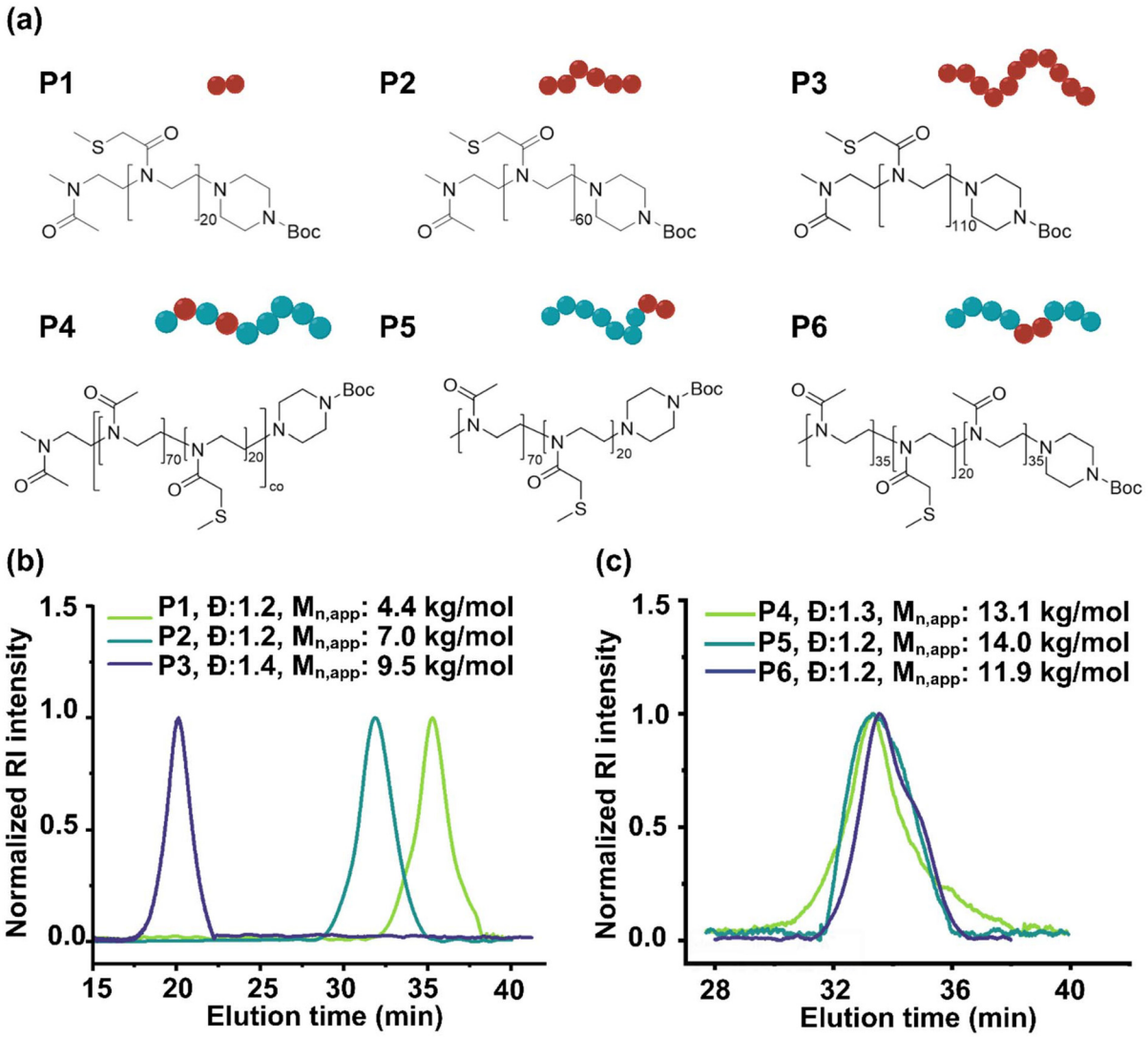

Fig. 1 (a) Chemical structures of the synthesized polymers. SEC traces of (b) pMeSMeOx$_{20}$ (**P1**), pMeSMeOx$_{60}$ (**P2**), pMeSMeOx$_{110}$ (**P3**), (c) pMeOx$_{70}$-*co*-pMeSMeOx$_{20}$ (**P4**), pMeOx$_{70}$-*b*-pMeSMeOx$_{20}$ (**P5**), and pMeOx$_{35}$-*b*-pMeSMeOx$_{20}$-*b*-pMeOx$_{35}$ (**P6**).

Table 1 Selected analytical data of the synthesized polymers

Polymer	$\bar{M}_n$ [a] (kg mol^{-1})	$\bar{M}_{n,app}$ [b] (kg mol^{-1})	$\bar{M}_n$ [c] (kg mol^{-1})	$Đ$ [b]	DP [a]
pMeSMeOx$_{20}$ (**P1**)	2.7	4.4	2.8	1.2	19
pMeSMeOx$_{60}$ (**P2**)	7.2	7.0	8.1	1.2	51
pMeSMeOx$_{110}$ (**P3**)	12	9.5	15	1.4	91
p(MeOx$_{70}$-*co*-MeSMeOx$_{20}$) (**P4**)	10	13	8.7	1.3	94
pMeOx$_{70}$-*b*-pMeSMeOx$_{20}$ (**P5**)	9.1	14	8.7	1.2	91
pMeOx$_{35}$-*b*-pMeSMeOx$_{20}$-*b*-pMeOx$_{35}$ (**P6**)	10	12	8.7	1.2	140

[a] Calculated *via* ^{1}H NMR end-group analysis. [b] Determined by SEC. [c] Calculated from the monomer/initiator concentration.

polymer analytical data is presented in the SI and summarized in Table 1.

To investigate whether the initiator salt approach enables polymerization with a reasonably living character without extensive chain transfer as reported by Kempe *et al.*,[53] we conducted kinetic studies of the MeSMeOx homopolymerization (Fig. 2a–d). Reactions were carried out under the same conditions as for **P2** (PMeSMeOx$_{60}$) synthesis (solvent ACN, 80 °C). The progress of the reactions was followed by ^{1}H NMR spectroscopy and SEC or by *in situ* IR spectroscopy, respectively. SEC revealed narrow molar mass distributions ($1.1 < Đ < 1.2$) and a linear increase of M_n with monomer conversion and

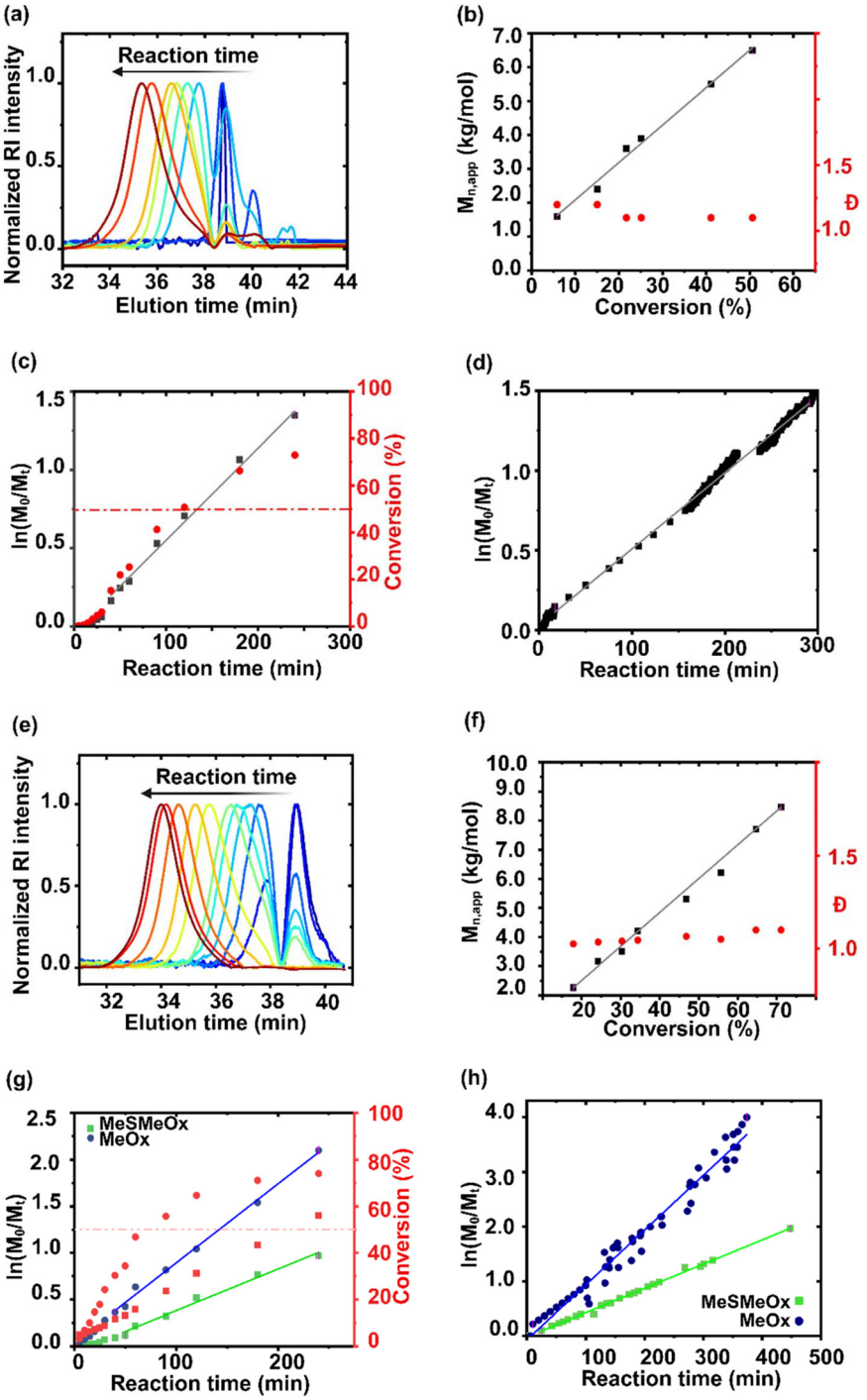

Fig. 2 (a–d) Kinetic study of MeSMeOx homopolymerization using MeMeOxOTf as a salt initiator in ACN at 80 °C (target DP = 60). (a) SEC elugrams of polymerization reaction controls taken after 0 (blue), 10, 30, 40, 50, 60, 90 and 120 min (red). (b) Evolution of number average molecular weight (M_n) and dispersity ($Đ$) as obtained by SEC with increasing MeSMeOx conversion. (c) Time-dependent monomer conversion and the corresponding ln[M_0]/[M_t]–time plot of MeSMeOx polymerization as determined by ^{1}H NMR analysis (slope = 0.0058 min^{-1}). (d) Time-dependent ln[M_0]/[M_t]–time plot of MeSMeOx polymerization as determined by *in situ* IR analysis following the reduction of the monomer signal at 960–980 cm^{-1} (slope = 0.0047 min^{-1}). (e–h) Kinetic study of MeOx : MeSMeOx (70 : 20) copolymerization using MeMeOxOTf as the salt initiator in ACN at 80 °C. (e) SEC elugrams of polymerization reaction controls taken after 0 (blue), 20, 30, 40, 50, 60, 90, 120, 180, 240 and 300 min (red). (f) Evolution of M_n and $Đ$ as obtained by SEC upon increasing monomer conversion. (g) Time-dependent MeOx and MeSMeOx conversion and the corresponding ln[M_0]/[M_t]–time plot of MeOx/MeSMeOx copolymerization as determined by ^{1}H NMR analysis (slope MeOx = 0.00849 min^{-1}, slope MeSMeOx = 0.0044 min^{-1}). (h) Time-dependent ln[M_0]/[M_t]–time plot of MeOx/MeSMeOx copolymerization as determined by *in situ* IR analysis following the reduction of the MeOx signal at 980 cm^{-1} and the MeSMeOx signal at 940–960 cm^{-1} (slope MeOx = 0.010 min^{-1}, slope MeSMeOx = 0.0044 min^{-1}) (in h and j: blue circles correspond to MeOx and green squares correspond to MeSMeOx).

Table 2 Propagation constants k_p for MeSMeOx homopolymerization using MeMeOxOTf as the salt initiator in ACN at 80 °C (target DP = 60) and MeOx/MeSMeOx copolymerization using MeMeOxOTf as the salt initiator in ACN at 80 °C (target DP_{MeOx} = 20, target $DP_{MeSMeOx}$ = 70)

Targeted polymer	Monomer	$[M]_0/[I]_0$	$k_{p,NMR}$ [10^{-3} L mol^{-1} s^{-1}]	$k_{p,IR}$ [10^{-3} L mol^{-1} s^{-1}]
$pMeSMeOx_{60}$	MeSMeOx	60	2.9	2.5
$p(MeOx_{70}$-*co*-$MeSMeOx_{20})$	MeOx	70	4.8	5.7
	MeSMeOx	20	2.5	2.5

reaction time (Fig. 2a and b). The semi-logarithmic pseudo-first order kinetic plot as determined by ^{1}H-NMR analysis shows a linear trend, implying a constant concentration of propagating species with a propagation constant $k_p = 2.9 \times 10^{-3}$ L mol^{-1} s^{-1} (Fig. 2c and Table 2). In addition, *in situ* IR spectra during MeSMeOx CROP show the evolution of signals attributable to the polymer (C═O (1650 cm^{-1}), N–C (1430 cm^{-1}) and C–C (1460–1480 cm^{-1})) as well as the reduction of signals attributed to the monomer (C–O (960–980 cm^{-1}) and N═C (1010 cm^{-1})) (Fig. S9a). In reasonable agreement with NMR data, the IR-derived semi-logarithmic plot of monomer consumption shows a linear trend corresponding to a k_p value of 2.5×10^{-3} L mol^{-1} s^{-1} (Fig. 2d and Table 2). Together, *in situ* IR and NMR analysis suggest good polymerization control and linear pseudo-first-order kinetics of MeSMeOx homopolymerization, while the linear increase of molar mass *vs.* monomer conversion, as obtained from SEC (Fig. 2b), suggests the absence of significant chain transfer. This implies that using the salt initiator approach, the CROP of MeSMeOx can indeed proceed in a reasonably living manner.

We further studied the kinetics of the copolymerization of MeOx and MeSMeOx performed to obtain **P4** P($MeOx_{70}$-*co*-$MeSMeOx_{20}$) (Fig. 2e–h). As before, the M_n values as determined by SEC increased with the reaction time and linearly with monomer conversion (Fig. 2e). Again, the corresponding elugrams reveal narrow molar mass distributions ($1.1 < Đ < 1.2$) (Fig. 2f). ^{1}H-NMR analysis revealed faster consumption of MeOx compared to MeSMeOx (Fig. 2g, $k_{p,MeOx} = 4.8 \times 10^{-3}$ L mol^{-1} s^{-1} *vs.* $k_{p,MeSMeOx} = 2.5 \times 10^{-3}$ L mol^{-1} s^{-1}) (Table 2). Similarly, upon tracking IR monomer signal reduction (940–960 cm^{-1} for MeSMeOx, 980 cm^{-1} for MeOx) (Fig. S10a), a linear pseudo-first-order kinetics is obtained for both monomers ($k_{p,MeOx} = 5.7 \times 10^{-3}$ L mol^{-1} s^{-1}, $k_{p,MeSMeOx} = 2.5 \times 10^{-3}$ L mol^{-1} s^{-1}) (Fig. 2h and Table 2). Taken together, SEC, ^{1}H NMR and *in situ* IR data imply that the copolymerization of MeOx and MeSMeOx proceeds in a living manner and results in a gradient architecture. More details on *in situ* IR are provided in the SI (Fig. S9 and S10).

To assess the thermal stability of polymers **P1–P6**, we conducted thermogravimetric analysis (TGA) under a normal and nitrogen atmosphere. For TGA curves in a nitrogen atmosphere, apart from a minor, steady loss at lower temperature, which is likely attributed to residual solvent and loss of Boc, the TGA thermograms imply high stability against temperature-induced degradation up to 300 °C for all synthesized polymers, similar to other POx. For the homopolymer **P1** with the lowest DP, the onset of degradation was found to be around 310 °C, while for homopolymers **P2** and **P3** with higher DP, a slightly higher onset of degradation of around 320 °C was determined (Fig. 3a). This indicates a minor effect of the molecular weight on the degradation temperature, but a more systematic study of this would be needed to confirm. The copolymers **P4–P6** exhibited an almost identical onset of degradation at around 320 °C (Fig. 3b).

Fig. S11 shows the thermal stability of the corresponding polymers under a normal atmosphere. Below 400 °C, all the decomposition patterns of the synthesized polymers are similar to those under nitrogen conditions, with minor changes in T_d, indicating the removal of absorbed water, organic solvents, and loss of Boc. However, as the temperature increases above 400 °C, all polymers undergo a slow and smooth weight loss. Because the sulfur group in the side chain can be oxidized under aerobic conditions, the residual weight percentages are not stabilized and continue to decrease throughout the entire temperature range.

Furthermore, differential scanning calorimetry (DSC) measurements were conducted. The thermograms revealed clear glass transition temperatures (T_g) for all synthesized homopolymers at approximately 40 °C for **P1**, 54 °C for **P2** and 63 °C for **P3** (Fig. 3c). Thus, as expected, a clear trend of increasing T_g with increasing DP was observed. Of note, Bener *et al.*[52] previously determined a T_g value of 48 °C for pMeSMeOx of DP = 100 (**P3**). We suspect that this lower T_g may be due to residual PEI units in PMeSMeOx, which can significantly decrease the T_g, even with a few units. All copolymers show a single T_g value of around 67 °C–69 °C (Fig. 3d), indicating the absence of (micro)phase separation. For the block copolymers **P5** and **P6**, in particular, this means that the individual blocks are miscible, probably due to their relatively short length. DSC thermograms do not display any other distinct features within the temperature range (−40 °C to 200 °C) studied. It can therefore be concluded that all synthesized polymers are purely amorphous in nature. However, with larger degrees of polymerization, we will expect microphase separation.

The amphiphilic block copolymers **P4**, **P5**, and **P6** are expected to self-assemble in selective solvents, such as water and might have utility in, *e.g.*, solubilization and ROS-triggered release of hydrophobic drugs. It should be noted that Bener *et al.*[52] realized similar amphiphilic ROS sensitive block copolymers with their approach, but arguably, our one-pot two step approach is more time and atom efficient. Accordingly, micelles were prepared using the thin film method (Scheme S2), commonly employed for POx-nanoformulation preparation.[61] Negative-stain TEM of aqueous polymer solu-

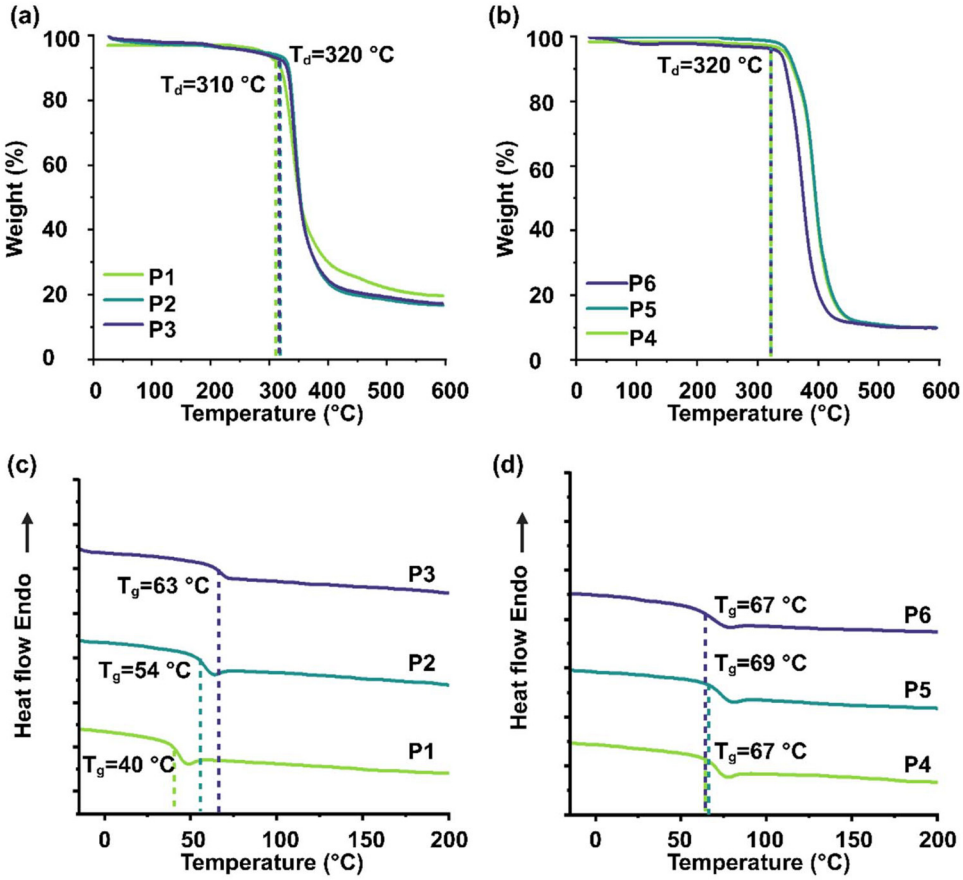

Fig. 3 TGA thermograms under a nitrogen atmosphere of (a) homopolymers **P1**, **P2** and **P3**, and of (b) copolymers **P4**, **P5** and **P6**. DSC curves of (c) homopolymers, **P1**, **P2** and **P3**, and of (d) copolymers **P4**, **P5** and **P6**.

tions (Fig. 4a) revealed that all three polymers formed spherical assemblies with particle diameters of 26 ± 5 nm for **P4**, 17 ± 5 nm for **P5**, and 21 ± 4 nm for **P6**, sizes that are consistent with the formation of simple spherical polymer micelles, as the theoretical extended chain lengths of the polymers are well below 50 nm. In contrast, SEM of aqueous polymer solutions at higher concentrations (Fig. 4b) revealed particle diameters of 195 ± 63 nm for **P4**, 224 ± 67 nm for **P5**, and 416 ± 96 nm for **P6**. Interestingly, DLS measurements at 45° scattering vector (room temperature) at 1 g L^{-1} (Fig. 4c and d after filtration through a hydrophilic 0.45 μm PTFE syringe filter, and Fig. S12 before filtration), performed after allowing the samples to equilibrate for 2 hours, further confirmed the presence of two narrowly distributed nanoparticle populations. Considering the intensity weighed distribution, we found sizes of 0.44 ± 0.11 μm, 0.43 ± 0.04 μm, and 0.54 ± 0.11 μm for **P4**, **P5** and **P6**, respectively (Fig. S12a). After filtration, the values decreased and the size distribution narrowed to 0.40 ± 0.04 μm, 0.42 ± 0.04 μm and 0.44 ± 0.02 μm for **P4**, **P5** and **P6**, respectively (Fig. 4c), indicating the removal of larger particles by filtration. In order to have a qualitative comparison with TEM results, BIC software uses a simple recalculation of intensity-to-number weighted distributions by dividing intensities by $(R_h^2)^x$, where x is a fractal dimension and equals 3 for a hard sphere. The number weighed distribution was centered around 18 ± 3 nm, 14 ± 3 nm and 37 ± 15 nm before filtration (Fig. S12b) and shifted to 21 ± 2 nm, 23 ± 7 nm and 55 ± 3 nm after filtration for **P4**, **P5** and **P6** (Fig. 4d), respectively. This indicates that filtration did not significantly affect the smaller particles but primarily removed the larger ones. These results suggest that the vast majority of self-assemblies are small, well-defined micelles with only a few submicron particles present. In addition, we conducted DOSY NMR spectroscopy (room temperature) at 10 g L^{-1}, which yielded even smaller hydrodynamic diameters of only 10 nm (more information regarding calculations is given in the SI and Table S4), highlighting the difficulties in accurately determining the sizes of self-assemblies, as different analytical techniques favor different populations. Overall, our findings suggest the formation of well-defined micelles of 25–50 nm with a very minor population of larger aggregates centered at around 0.4 μm.

To further investigate the self-assembly of the amphiphilic copolymers, we employed AF4. This method allows the gentle, diffusion-based separation of the differently sized species in the AF4 channel. We focused on **P4** since we encountered solubility issues of **P5** and **P6** in the AF4 eluent. We were able to

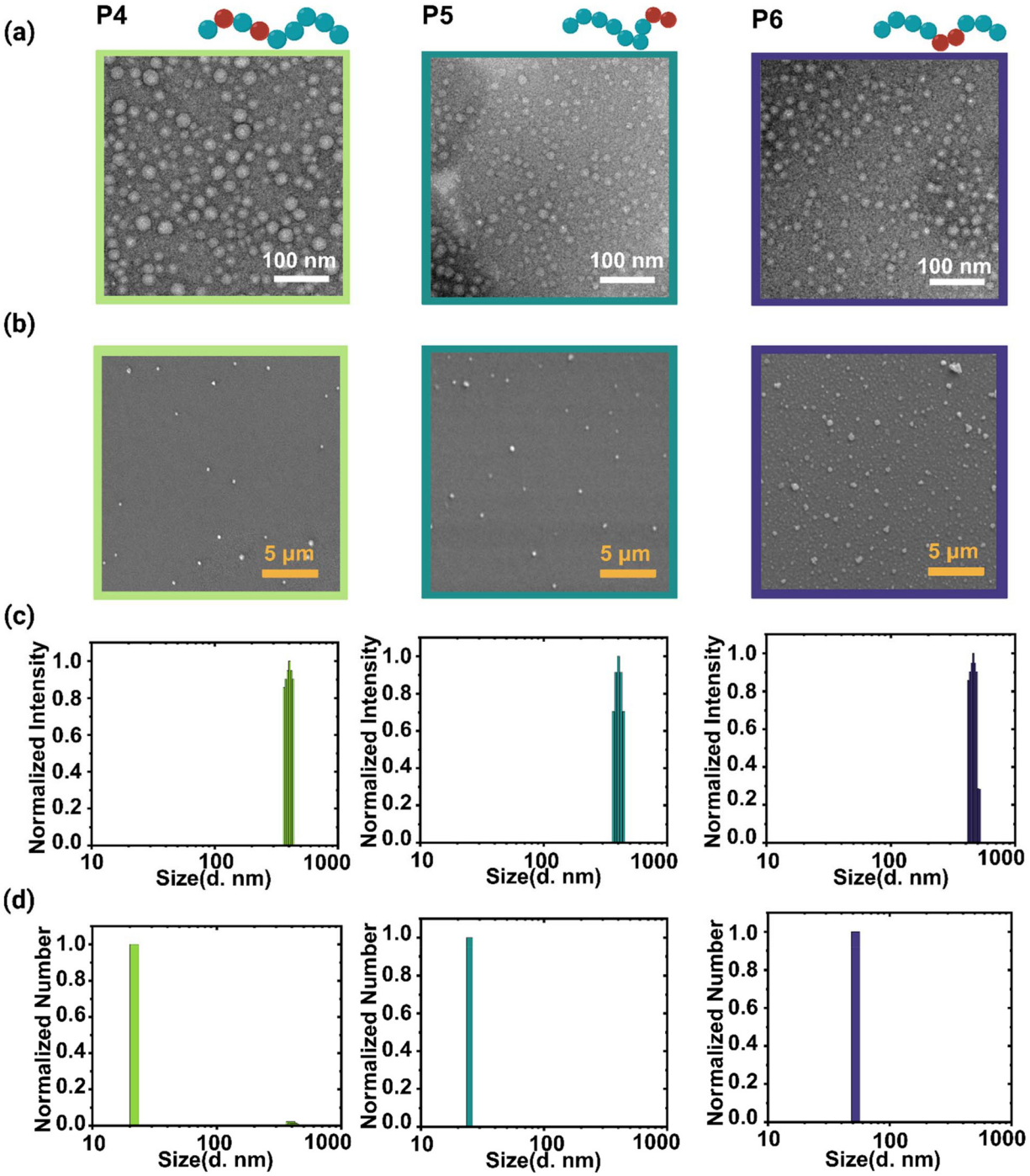

Fig. 4 (a) Negative stain TEM images of diluted (1 : 125) aqueous polymer solutions (c = 20 g L^{-1}) of **P4**, **P5** and **P6** after incubation on the grids for 1 min before blotting (white scale bar = 100 nm), (b) SEM images of aqueous polymer solutions (c = 1 g L^{-1}) of **P4**, **P5** and **P6** (orange scale bar = 5 μm), (c), and (d) The size distribution by intensity and number, respectively (measured at 45° scattering vector) of **P4**, **P5**, and **P6** (1 g L^{-1}) in diH_2O (2 mM $NaNO_3$) (filtered through a hydrophilic 0.45 μm PTFE syringe filter).

separate two distinct fractions in the solution of the amphiphilic polymer P4 (Fig. S13a and Table S5). The first fraction elutes directly after the void peak between 6 and 9 minutes of the measurement. This species shows an intense signal in the concentration-based UV and dRI detectors, indicating that this is the main fraction present in the sample solution. The relative LS intensity for this fraction is too low to obtain reliable size determination results. We attribute this fraction to the smaller micellar fraction in the sample, which was observed in TEM imaging and the number-weighed DLS distribution. The second fraction elutes between 20 and 30 minutes of the measurement. Here, the low relative intensity in the concen-

tration-based detectors indicates that this species only exists in a low quantity in the sample solution. The high relative LS intensity allows one to determine a radius of gyration of 194 nm using the Berry model. Overall, this indicates that the second fraction is the larger species which exists in a low concentration in the sample solution. Again, this corroborates the observation and corresponding interpretation of TEM, SEM and DLS data. Everything eluting after 30 minutes is likely aggregates which form during the focusing step of the measurement. Thus, AF4 confirms the existence of two differently sized self-assembly species within the sample.

The concentration-based UV/VIS and dRI detectors can be used to assess the ratio of the two species in solution. Importantly, these values are approximations because the integral intensities of either fraction could be influenced by aggregation in the channel as well as the overall mass recovery. Nonetheless, based on the integral intensity-based calculation, the main fraction makes up 98.5% (dRI) or 95% (UV/Vis) of the sample while only accounting for approx. 2.2% of light scattering intensity. Therefore, AF4 also indicates that the majority of self-assemblies are small micelles, while the larger species only exists in a low concentration.

For use as stimuli-responsive biomaterials, suitable safety is required, with cytocompatibility being the primary concern. To assess the impact of the amphiphilic PMeSMeOx-based copolymers **P4–P6** on cell viability of the NIH/3T3 fibroblast cell line, we performed a CellTiter-Glo® assay. This assay evaluates cell viability by measuring ATP levels, which reflect metabolically active cells.[62] The fibroblast cells were incubated with amphiphilic polymer (**P4–P6**) over a wide range of concentrations (0.003 g L^{-1}–100 g L^{-1}) for 24 h and 72 h, respectively. At 24 h incubation, high cell viability (>80%) was observed up to a polymer concentration of 3 g L^{-1} for all polymers (Fig. 5a). For the block copolymers **P5** and **P6**, the half-maximum inhibitory concentration (IC_{50}) was found to be around 50 g L^{-1}. The gradient copolymer **P4** was only slightly less well tolerated by the fibroblasts ($IC_{50} \approx 20$ g L^{-1}). This minor difference based on the copolymer architecture could indicate differences in the cell membrane interactions and endocytosis,[63] which should be studied in more detail. In the case of **P5** and **P6**, the situation is essentially unchanged after 72 h, with high cell viability up to a concentration of 10 g L^{-1}. Equally similar, the gradient copolymer **P4** showed a slightly higher cytotoxicity, starting around a concentration of 3 g L^{-1} (>75% cell viability) and an IC_{50} value of 20 g L^{-1}. Taken together, the CellTiter-Glo® assay revealed only minor differences between the polymers and high IC_{50} values.

The underlying rationale for the presently discussed polymers is their use as oxidation-responsive biomaterials.[64,65] Upon exposure to ROS, such as H_2O_2 or other ROS species produced in an inflamed tissue, thioether groups can be oxidized to sulfoxides and finally to sulfones (Fig. 6a, and Scheme S3). To investigate how oxidative conditions influence the hydrophobic to hydrophilic transition of $PMeSMeOx_{20}$ (**P1**), the polymer was incubated at four different concentrations of H_2O_2 (0 M, 10 nM, 100 μM, and 10 mM) at a fixed polymer concentration of 10 g L^{-1} for 5 days. Visual inspection (Fig. S13) revealed rapid dissolution at higher oxidative strengths; specifically, complete dissolution occurred within 2 hours at 10 mM H_2O_2. In contrast, dissolution was significantly delayed (up to 5 days) at 100 μM H_2O_2. At the lowest tested concentration (10 nM) and in diH_2O, the polymer remained insoluble after 5 days, although partial swelling was evident in diH_2O. To further elucidate the oxidative transformation of **P1**, the samples were characterized by SEC and ^{1}H NMR following the incubation period. SEC revealed an increase in dispersity ($Đ \approx 1.4$) across all polymer samples following incubation with H_2O_2. Notably, the elution times remained unchanged, indicating that no significant degradation occurred under oxidative conditions (Fig. 6b, Table 3). This observation is further supported by ^{1}H NMR spectroscopy, which showed that the degree of polymerization (DP) remained approximately consistent across samples treated with varying concentrations of H_2O_2. In the ^{1}H NMR spectra,

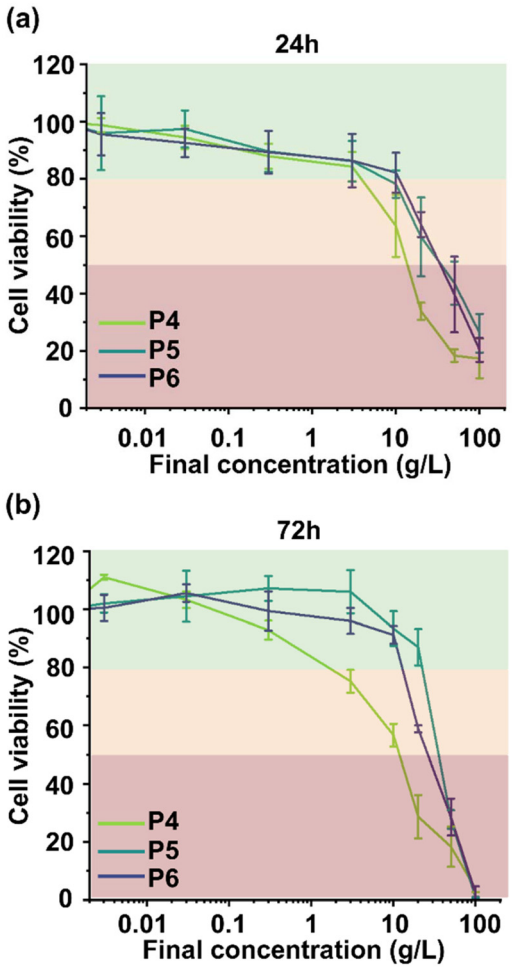

Fig. 5 Cell viability of block copolymers as assessed by the CellTiter-Glo® assay, (a) 24 h, and (b) 72h after incubation of the NIH/3T3 cell line with block copolymer micelles. Values presented are means ± standard deviation from two biological replicates, each with three technical replicates.

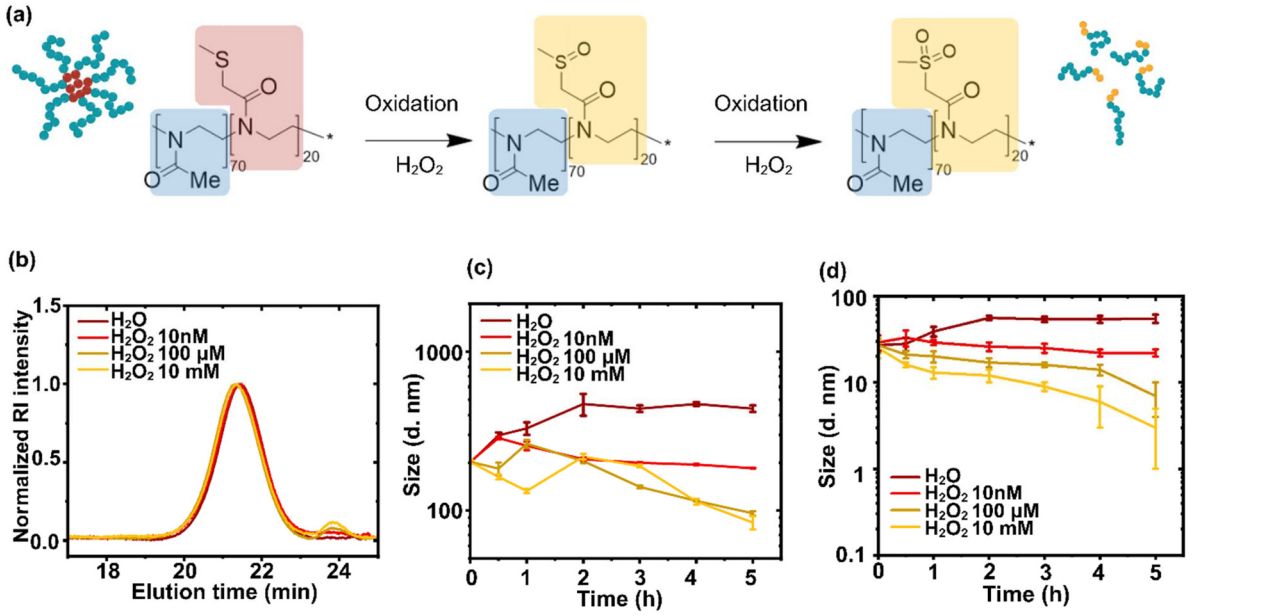

Fig. 6 (a) Schematic illustration of the oxidative reaction of thioether-bearing POx with H_2O_2. (b) SEC traces (HFIP as the solvent) of $PMeSMeOx_{20}$ (**P1**) and its oxidation products after treatment with hydrogen peroxide (H_2O_2) at varying concentrations (0 M, 10 nM, 100 μM, and 10 mM) over a period of 5 days. The size distribution by (c) intensity and (d) number (measured at 45° scattering vector) of **P6** (1 g L^{-1}) in diH_2O (2 mM $NaNO_3$) after oxidation by H_2O_2 at varying concentrations (0 M, 10 nM, 100 μM, and 10 mM) over 5 hours (filtered through a hydrophilic 0.45 μm PTFE syringe filter).

Table 3 Selected analytical data of oxidation of $PMeSMeOx_{20}$ (**P1**) after incubation (concentration of 10 g L^{-1}) in the presence of hydrogen peroxide (H_2O_2) at varying concentrations (0 M, 10 nM, 100 μM, and 10 mM) over a period of 5 days

	Before incubation	H_2O_2 (0 M)	H_2O_2 (10 nM)	H_2O_2 (100 μM)	H_2O_2 (10 mM)
$\bar{M}_n$ [a] (kg mol^{-1})	2.9	2.9	3.1	3.1	3.5
$\bar{M}_{n,app}$ [b] (kg mol^{-1})	4.4	4.1	4.0	4.4	4.3
$Đ$[b]	1.2	1.4	1.4	1.4	1.4
DP[a]	20	20	21	20	22
Oxidation to sulfoxide%[a]	—	0	14	45	86
Oxidation to sulfone%[a]	—	0	0	10	9

[a] Calculated *via* ^{1}H NMR end-group analysis. [b] Determined by SEC.

characteristic downfield shifts were observed for both the methyl (CH_3–S) and methylene (CH_2–S) groups in the side chain upon oxidation. Specifically, oxidation to the sulfoxide led to shifts of approximately 0.5 ppm, with the CH_3–S resonance moving from 2.0 to 2.6 ppm and the CH_2–S resonance from 3.5 to 4.0 ppm. At higher oxidation levels, further conversion to the sulfone resulted in shifts of approximately 1.0 ppm, with the CH_3–S peak shifting from 2.0 to 3.1 ppm and the CH_2–S peak from 3.5 to 4.5 ppm. These chemical shift changes are consistent with the oxidation of the thioether groups (Fig. S15 and Table 3). IR analysis further supported these findings, showing characteristic S–C deformation bands (~880 and 1465 cm^{-1}) and an S=O stretching band (~1000 cm^{-1}) upon oxidation. Importantly, a distinct S=O stretching band attributed to sulfone (R–SO_2–R′) at ~1080 cm^{-1} was only detected at higher oxidant concentrations (10 μM and 100 mM H_2O_2), confirming the stepwise progression from sulfoxide to sulfone in the thioether side chains (Fig. S16). These findings demonstrate that $PMeSMeOx_{20}$ (**P1**) exhibits a concentration dependent oxidative response to H_2O_2, undergoing structural and solubility changes indicative of sulfoxide and sulfone formation.

In the case of amphiphilic self-assemblies formed by the copolymers **P4–P6**, exposure to ROS is expected to induce disassembly, as the hydrophobic block is rendered hydrophilic. To test the ROS-responsive behavior, we treated **P6** with four different concentrations of H_2O_2 (0 M, 10 nM, 100 μM, and 10 mM) over a period of 5 hours and monitored the size (d, nm) of self-assembled polymers as a function of incubation time and concentrations of H_2O_2 (intensity weighed distribution in Fig. 6c and number weighed distribution in Fig. 6d). DLS measurements revealed a clear, concentration dependent disassembly behavior of the **P6** based assemblies in response to H_2O_2. In the absence of H_2O_2, the assemblies remained

stable, with a slight increase in the particle size over time, likely attributable to core swelling, a phenomenon also observed for **P1** (Fig. S11). This swelling was evident across all H_2O_2 concentrations; however, at higher concentrations of H_2O_2, the rate of disassembly was faster than swelling. Treatment with 10 nM H_2O_2 led to a modest decrease in the intensity weighted particle size. This effect became more pronounced at higher concentrations: at 100 μM and 10 mM H_2O_2, particle size decreased rapidly and substantially over the 5-hour period, consistent with efficient ROS induced disassembly. The most rapid and extensive disassembly was observed at 10 mM H_2O_2, where particle sizes fell below 100 nm in intensity weighed distribution and below 5 nm in number weighed distribution, showing that the decrease in size is not only for few large particles but also for smaller single assemblies with the incubation time and concentration of H_2O_2. These results confirm the ROS responsiveness of **P6** assemblies and highlight their potential for use in stimuli-responsive nanomaterials and drug delivery systems. Notably, the 10 nM and 100 μM H_2O_2 concentrations are physiologically relevant, as H_2O_2 levels in healthy tissue are typically below 10 nM and can increase to approximately 100 μM under inflammatory conditions.[24]

Conclusion

For the first time, well-defined thioether-bearing poly(2-oxazoline)s (PMeSMeOx) were successfully polymerized in a controlled manner through cationic ring-opening polymerization of thioether bearing monomers. Key was the use of an initiator salt (MeMeOxOTf), while the block polymers of MeOx and MeSMeOx were synthesized by MeOTf. The introduction of thioether groups into the polymer backbone has been shown to impart significant sensitivity to reactive oxygen species. Supported by FTIR, SEC, ^{1}H NMR and DLS analyses, we demonstrate that the thioether-functionalized poly(2-oxazoline)s exhibit a responsive disassembly in the presence of ROS, indicating their potential utility as smart materials for targeted drug delivery systems, where controlled release in oxidative environments is desirable. This simple new approach offers improved atom economy and simpler access to complex polymer architectures compared to previous methods. Future research should focus on exploring the *in vivo* biocompatibility and the controlled release of compounds of interest to better understand their practical applications and limitations. Overall, our study highlights the promising potential of thioether-bearing poly(2-oxazoline)s in the realm of responsive polymers and sets the stage for further exploration into their applications in advanced materials science and biomedicine.

Author contributions

The manuscript was written through contributions of all authors. All authors have given approval to the final version of the manuscript.

Conflicts of interest

The authors declare no conflicts of interest.

Data availability

The data supporting this article have been included as part of the supplementary information (SI). More information on all data presented in this article are available at Zenodo at https://zenodo.org/records/17356185. The Supplementary Information file includes additional datasets, figures, and tables supporting the findings of this study. See DOI: https://doi.org/10.1039/d5py00659g.

Acknowledgements

S. N. M. acknowledges financial support through the MATRENA (Materials Research and Nanoscience) doctoral programme at the University of Helsinki. A.-L. Z. appreciates financial support through the CHEMS (Chemistry and Molecular Sciences) doctoral programme at the University of Helsinki. The authors thank Mirkka Sarparanta for access to cell culture facilities and Timo Repo for access to *in situ* IR. Furthermore, we acknowledge the support from Sami-Pekka Hirvonen and Andrew Kerr for SEC measurements and Vladimir Aseyev for DLS analysis.

References

1 S. Chatterjee and P. Chi-leung Hui, Review of stimuli-responsive polymers in drug delivery and textile application, *Molecules*, 2019, **24**(14), 2547.
2 C. M. Wells, *et al.*, Stimuli-responsive drug release from smart polymers, *J. Funct. Biomater.*, 2019, **10**(3), 34.
3 S. S. Das, *et al.*, Stimuli-responsive polymeric nanocarriers for drug delivery, imaging, and theragnosis, *Polymers*, 2020, **12**(6), 1397.
4 Y. Lu, W. Sun and Z. Gu, Stimuli-responsive nanomaterials for therapeutic protein delivery, *J. Controlled Release*, 2014, **194**, 1–19.
5 P. Mahlumba, *et al.*, Stimuli-responsive polymeric systems for controlled protein and peptide delivery: future implications for ocular delivery, *Molecules*, 2016, **21**(8), 1002.
6 Y. Li, *et al.*, *Stimuli-responsive polymeric nanocarriers for efficient gene delivery*, in *Polymeric Gene Delivery Systems*, 2018, pp. 167–215.
7 N. K. Preman, *et al.*, Recent developments in stimuli-responsive polymer nanogels for drug delivery and diagnostics: A review, *Eur. J. Pharm. Biopharm.*, 2020, **157**, 121–153.
8 A. Balcerak-Woźniak, M. Dzwonkowska-Zarzycka and J. Kabatc-Borcz, A Comprehensive Review of Stimuli-Responsive Smart Polymer Materials—Recent Advances and Future Perspectives, *Materials*, 2024, **17**(17), 4255.

9 F. Farjadian, *et al.*, Physically stimulus-responsive nanoparticles for therapy and diagnosis, *Front. Chem.*, 2022, **10**, 952675.
10 F. F. Sahle, M. Gulfam and T. L. Lowe, Design strategies for physical-stimuli-responsive programmable nanotherapeutics, *Drug Discovery Today*, 2018, **23**(5), 992–1006.
11 J. R. Lopes, *et al.*, Physical and chemical stimuli-responsive drug delivery systems: targeted delivery and main routes of administration, *Curr. Pharm. Des.*, 2013, **19**(41), 7169–7184.
12 M. Gulfam, F. F. Sahle and T. L. Lowe, Design strategies for chemical-stimuli-responsive programmable nanotherapeutics, *Drug Discovery Today*, 2019, **24**(1), 129–147.
13 F. H. Sobotta, *et al.*, Oxidation-responsive micelles by a one-pot polymerization-induced self-assembly approach, *Polym. Chem.*, 2018, **9**(13), 1593–1602.
14 M. Shahriari, *et al.*, Enzyme responsive drug delivery systems in cancer treatment, *J. Controlled Release*, 2019, **308**, 172–189.
15 M. Zhang, *et al.*, Advanced application of stimuli-responsive drug delivery system for inflammatory arthritis treatment, *Mater. Today Bio*, 2022, **14**, 100223.
16 J. Majumder and T. Minko, Multifunctional and stimuli-responsive nanocarriers for targeted therapeutic delivery, *Expert Opin. Drug Delivery*, 2021, **18**(2), 205–227.
17 S. Municoy, *et al.*, Stimuli-responsive materials for tissue engineering and drug delivery, *Int. J. Mol. Sci.*, 2020, **21**(13), 4724.
18 A. R. Salgarella, *et al.*, Investigation of drug release modulation from poly (2-oxazoline) micelles through ultrasound, *Sci. Rep.*, 2018, **8**(1), 9893.
19 S. H. Lee, *et al.*, Current progress in reactive oxygen species (ROS)–responsive materials for biomedical applications, *Adv. Healthcare Mater.*, 2013, **2**(6), 908–915.
20 A. van der Vliet and Y. M. Janssen-Heininger, Hydrogen peroxide as a damage signal in tissue injury and inflammation: murderer, mediator, or messenger?, *J. Cell. Biochem.*, 2014, **115**(3), 427–435.
21 Y. Yang and W. Sun, Recent advances in redox-responsive nanoparticles for combined cancer therapy, *Nanoscale Adv.*, 2022, **4**(17), 3504–3516.
22 C. Lennicke, *et al.*, Hydrogen peroxide–production, fate and role in redox signaling of tumor cells, *Cell Commun. Signaling*, 2015, **13**, 1–19.
23 R. Gaikwad, P. Thangaraj and A. Sen, Direct and rapid measurement of hydrogen peroxide in human blood using a microfluidic device, *Sci. Rep.*, 2021, **11**(1), 2960.
24 C. H. Coyle, *et al.*, Mechanisms of H_2O_2-induced oxidative stress in endothelial cells, *Free Radicals Biol. Med.*, 2006, **40**(12), 2206–2213.
25 B. Halliwell, M. V. Clement and L. H. Long, Hydrogen peroxide in the human body, *FEBS Lett.*, 2000, **486**(1), 10–13.
26 J. Liang and B. Liu, ROS–responsive drug delivery systems, *Bioeng. Transl. Med.*, 2016, **1**(3), 239–251.
27 E. Lallana and N. Tirelli, Oxidation–responsive polymers: Which groups to use, how to make them, what to expect from them (biomedical applications), *Macromol. Chem. Phys.*, 2013, **214**(2), 143–158.
28 I. Piergentili, *et al.*, Thioanisole ester based logic gate cascade to control ROS-triggered micellar degradation, *Polym. Chem.*, 2022, **13**(16), 2383–2390.
29 M. K. Gupta, *et al.*, Poly (PS-b-DMA) micelles for reactive oxygen species triggered drug release, *J. Controlled Release*, 2012, **162**(3), 591–598.
30 A. Napoli, *et al.*, Oxidation-responsive polymeric vesicles, *Nat. Mater.*, 2004, **3**(3), 183–189.
31 P. Hu and N. Tirelli, Scavenging ROS: superoxide dismutase/catalase mimetics by the use of an oxidation-sensitive nanocarrier/enzyme conjugate, *Bioconjugate Chem.*, 2012, **23**(3), 438–449.
32 N. Ma, *et al.*, Selenium-containing block copolymers and their oxidation-responsive aggregates, *Polym. Chem.*, 2010, **1**(10), 1609–1614.
33 P. Han, *et al.*, Red light responsive diselenide-containing block copolymer micelles, *J. Mater. Chem. B*, 2013, **1**(6), 740–743.
34 K. E. Broaders, S. Grandhe and J. M. Fréchet, A biocompatible oxidation-triggered carrier polymer with potential in therapeutics, *J. Am. Chem. Soc.*, 2011, **133**(4), 756–758.
35 D. S. Wilson, *et al.*, Orally delivered thioketal nanoparticles loaded with TNF-α–siRNA target inflammation and inhibit gene expression in the intestines, *Nat. Mater.*, 2010, **9**(11), 923–928.
36 S. S. Yu, *et al.*, Physiologically relevant oxidative degradation of oligo (proline) cross-linked polymeric scaffolds, *Biomacromolecules*, 2011, **12**(12), 4357–4366.
37 S. Kim, *et al.*, Polyoxalate nanoparticles as a biodegradable and biocompatible drug delivery vehicle, *Biomacromolecules*, 2010, **11**(3), 555–560.
38 M. Criado-Gonzalez and D. Mecerreyes, Thioether-based ROS responsive polymers for biomedical applications, *J. Mater. Chem. B*, 2022, **10**(37), 7206–7221.
39 L. Yu, *et al.*, ROS-responsive poly (ε-caprolactone) with pendent thioether and selenide motifs, *Polym. Chem.*, 2018, **9**(27), 3762–3773.
40 T. Lorson, *et al.*, Poly(2-oxazoline)s based biomaterials: A comprehensive and critical update, *Biomaterials*, 2018, **178**, 204–280.
41 R. Luxenhofer, *et al.*, Poly (2−oxazoline) s as Polymer Therapeutics, *Macromol. Rapid Commun.*, 2012, **33**(19), 1613–1631.
42 M. Glassner, M. Vergaelen and R. Hoogenboom, Poly(2-oxazoline)s: A comprehensive overview of polymer structures and their physical properties, *Polym. Int.*, 2018, **67**(1), 32–45.
43 B. Verbraeken, *et al.*, *The Chemistry of Poly(2-oxazoline)s, in Encyclopedia of Polymer Science and Technology*, 2017, pp. 1–59.
44 M. Bauer, *et al.*, Poly(2-ethyl-2-oxazoline) as Alternative for the Stealth Polymer Poly(ethylene glycol): Comparison of in vitro Cytotoxicity and Hemocompatibility, *Macromol. Biosci.*, 2012, **12**(7), 986–998.

45 R. Luxenhofer and R. Jordan, Poly (2-oxazoline) s (POx) in Biomedical Applications, *Mater. Matters*, 2013, **8**, 70–73.
46 M. Barz, *et al.*, Overcoming the PEG-addiction: well-defined alternatives to PEG, from structure–property relationships to better defined therapeutics, *Polym. Chem.*, 2011, **2**(9), 1900–1918.
47 Z. He, *et al.*, A high capacity polymeric micelle of paclitaxel: Implication of high dose drug therapy to safety and in vivo anti-cancer activity, *Biomaterials*, 2016, **101**, 296–309.
48 M. M. Lübtow, *et al.*, More Is Sometimes Less: Curcumin and Paclitaxel Formulations Using Poly (2−oxazoline) and Poly (2−oxazine)–Based Amphiphiles Bearing Linear and Branched C9 Side Chains, *Macromol. Biosci.*, 2018, **18**(11), 1800155.
49 R. Hoogenboom, *et al.*, Microwave-assisted synthesis and properties of a series of poly(2-alkyl-2-oxazoline)s, *Des. Monomers Polym.*, 2005, **8**(6), 659–671.
50 A. Zahoranová and R. Luxenhofer, Poly(2-oxazoline)- and Poly(2-oxazine)-Based Self-Assemblies, Polyplexes, and Drug Nanoformulations—An Update, *Adv. Healthcare Mater.*, 2021, **10**(6), 2001382.
51 E. Vlassi, A. Papagiannopoulos and S. Pispas, Amphiphilic poly(2-oxazoline) copolymers as self-assembled carriers for drug delivery applications, *Eur. Polym. J.*, 2017, **88**, 516–523.
52 S. Bener, *et al.*, Thioether-based poly (2-oxazoline) s: from optimized synthesis to advanced ROS-responsive nanomaterials, *Polym. Chem.*, 2023, **14**(42), 4838–4847.
53 K. Kempe, *et al.*, Synthesis and characterization of a series of diverse poly (2−oxazoline) s, *J. Polym. Sci., Part A: Polym. Chem.*, 2009, **47**(15), 3829–3838.
54 H. Witte and W. Seeliger, Simple synthesis of 2-substituted 2-oxazolines and 5, 6-dihydro-4H-1, 3-oxazines, *Angew. Chem., Int. Ed. Engl.*, 1972, **11**(4), 287–288.
55 S. Kobayashi, *et al.*, Synthesis of a nonionic polymer surfactant from cyclic imino ethers by the initiator method, *Macromolecules*, 1987, **20**(8), 1729–1734.
56 P. Persigehl, R. Jordan and O. Nuyken, Functionalization of amphiphilic poly (2-oxazoline) block copolymers: A novel class of macroligands for micellar catalysis, *Macromolecules*, 2000, **33**(19), 6977–6981.
57 K. Lüdtke, *et al.*, Lipopolymers from New 2−Substituted–2−Oxazolines for Artificial Cell Membrane Constructs, *Macromol. Biosci.*, 2005, **5**(5), 384–393.
58 M. M. Lübtow, *et al.*, Drug specificity, synergy and antagonism in ultrahigh capacity poly (2-oxazoline)/poly (2-oxazine) based formulations, *J. Am. Chem. Soc.*, 2017, **139**(32), 10980–10983.
59 C. Taubmann, *et al.*, First Aldehyde–Functionalized Poly (2-oxazoline) s for Chemoselective Ligation, *Macromol. Biosci.*, 2005, **5**(7), 603–612.
60 H. Witte and W. Seeliger, Cyclische imidsäureester aus nitrilen und aminoalkoholen, *Justus Liebigs Ann. Chem.*, 1974, **1974**(6), 996–1009.
61 R. Luxenhofer, *et al.*, Doubly amphiphilic poly (2-oxazoline) s as high-capacity delivery systems for hydrophobic drugs, *Biomaterials*, 2010, **31**(18), 4972–4979.
62 S. Imlimthan, *et al.*, Systematic in vitro biocompatibility studies of multimodal cellulose nanocrystal and lignin nanoparticles, *J. Biomed. Mater. Res., Part A*, 2020, **108**(3), 770–783.
63 M. Barz, *et al.*, The uptake of N-(2-hydroxypropyl)-methacrylamide based homo, random and block copolymers by human multi-drug resistant breast adenocarcinoma cells, *Biomaterials*, 2009, **30**(29), 5682–5690.
64 A. Siani, *et al.*, Polysulfide nanoparticles inhibit fibroblast-to-myofibroblast transition via extracellular ROS scavenging and have potential anti-fibrotic properties, *Biomater. Adv.*, 2023, **153**, 213537.
65 F. El-Mohtadi, R. d'Arcy and N. Tirelli, Oxidation–Responsive Materials: Biological Rationale, State of the Art, Multiple Responsiveness, and Open Issues, *Macromol. Rapid Commun.*, 2019, **40**(1), 1800699.